



Effect of heat treatment on anisotropic mechanical properties of 316L stainless steel produced via laser-based powder bed fusion

Reza Sedaghat, Yousef Mazaheri*, Nozar Anjabin, Ramin Ebrahimi

Department of Materials Science and Engineering, School of Engineering, Shiraz University, Shiraz 71946-84334, Iran

Received: 24 December 2024; Accepted: 10 February 2025

*Corresponding author, E-mail: yousef.mazaheri@shirazu.ac.ir

ABSTRACT

In this study, the AISI 316L stainless steel samples produced by the laser-based powder bed fusion (LPBF) process were subjected to annealing at temperatures of 900°C, 1000°C, and 1100°C for holding times up to 6h. The impact of annealing treatment on the evolution of microstructure, hardness, and anisotropy in different planes of the samples was systematically investigated. The findings revealed that after annealing at 900°C for 3h, melt pool boundaries remained visible, indicating incomplete diffusion under these conditions. However, at constant temperature increasing the annealing duration to 4h, resulted in the disappearing of melt pool boundaries, and reducing the average hardness values from 256, 271, 242 HV0.2 to 195, 198, and 205 HV0.2 in TD-ND, TD-BD, and BD-ND planes, respectively. The same behavior was also achieved by annealing at higher temperatures of 1000°C and 1100°C. In addition, by increasing the holding time over 4h, the average hardness raised slowly for all samples, which may be related to the accumulation of carbide particles at grains and grain boundaries that restricts the grain boundary motion. Furthermore, increasing the annealing temperature to 1000°C and 1100°C for 4h led to the formation of annealing twins and complete transformation of columnar grains into equiaxed grains, as observed in the microstructure. A comparison of the microstructure and hardness values (186-188HV0.2) confirmed that full recrystallization and the elimination of anisotropy were achieved after annealing at 1100°C for 4h due to the formation of new recrystallized grains, annihilation of cell structures and complete dissolution of melt pool boundaries.

Keywords: Laser-based powder bed fusion (LPBF); 316L stainless steel; Annealing treatment; Mechanical properties anisotropy.

1. Introduction

AISI 316L stainless steel has numerous applications in various industries such as automotive, aerospace, petrochemical sectors, nuclear, and biomedical applications owing to its cost-effectiveness and, superior mechanical properties in conditions ranging from high to very low temperatures [1-3], high formability and weldability [4]. Moreover, the presence of chromium and molybdenum elements in 316L stainless steel enhances both its corrosion resistance in chloride environments and its performance at elevated temperatures [3, 5, 6]. Additive manufacturing

(AM) has expanded beyond its original application in prototyping to produce manufacture with shapes that closely resemble their final forms. AM presents a competitive alternative to conventional manufacturing processes such as casting, forging, and sintering requiring significant financial and considerable time investments [7, 8]. This technique has gained unique advantages for 316L stainless steel and it has been developed dramatically throughout recent years, especially the laser-based powder bed fusion (LPBF) technique [9, 10] which is used for producing nearly complete density [11], considerably reducing in mass [12] and advanced

structural shapes and geometries [13]. This technique involves targeting the powder layer with a high-energy laser beam, enabling the powder particles to absorb energy through bulk, and powder coupling will occur and induce the formation of a molten pool. The distinctive properties of AM parts, such as anisotropy and inhomogeneity are a result of their layer-wise formation and location-specific alternations during extended periods at elevated temperatures [14]; moreover, the fabrication of AM components involves a complex epitaxial thermal journey, resulting in build orientation dependency attributed to heterogeneity and anisotropy [15, 16]. Taghipour et al. [17] investigated the dependency of strain hardening behavior of LPBF-316L stainless steel on different building orientations and reported that the uniaxial tensile specimens were produced in horizontal and vertical orientations parallel to the building platform and building direction respectively. Vertical samples experienced higher elongation, but lower yield and ultimate tensile strength compared to the horizontal samples. Also, the work hardening exponent values of the 316L stainless steel samples produced by laser powder bed fusion showed a significant dependency on orientation; which was in complete agreement with Kumar et al. [18]. Mower and Long [19] investigated the influence of build orientation and surface roughness of metallic alloys such as stainless steel 316L produced via LPBF. Their findings indicated that materials constructed horizontally exhibited longer fatigue lives compared to those built vertically. It is worth noting that the anisotropic and heterogeneous characteristics of metal AM components also arise from defects such as pores, lack of fusion layers, and surface roughness [20]. Some studies also reported that anisotropy could be caused by various factors, including scan strategy, grain growth direction during solidification, and the formation of numerous oxides between layers [21, 22]. For example, Hitzler et al. [23] explored the anisotropic tensile strength of stainless steel fabricated using selective laser melting. They highlighted that the observations about the material's behavior based on orientation were noticeably different and often contradictory. They showed that although the layers that were parallel to the loading directions experienced the highest elongation to failure, the maximum elongation after fracture was found in specimens with layers arranged perpendicular to the loading direction.

Also, Morozova et al. [24] investigated the effect of annealing at various temperatures (650, 850, 1050, and 1100°C) and different durations (10 and 60 min). The findings showed that annealing treatment at 1100°C for 60 minutes led to the elimination of microstructural anisotropy resulting in a more homogeneous microstructure. In addition, following the fabrication of samples via the LPBF process, a series of post-processing steps need to be conducted, one of which is annealing. This treatment enhances the properties of printed samples by adjusting the microstructure through recovery or recrystallization [25]. For example, Chao et al. [26] highlighted the effect of annealing over a wide temperature range of 400 - 1400°C with various holding times. According to the results, the recrystallization of columnar grains, grain growth, and increase in the size of oxide particles were evident by annealing at 1100°C for 8h. Wang et al. [27] studied the effect of holding times (1h, 2h, 3h, and 6h) at 1000°C on 316L stainless steel samples. After 3h annealing, minor recrystallized grains with oxide particles and dissolved dislocations were observed in the microstructure; however, the structure was near full recrystallization after annealing for 6h.

Up to now, few investigations have studied the effect of post-manufacturing heat treatment (PMHT) on the anisotropic behavior of 316L stainless steel samples fabricated by the LPBF process. Therefore, we focus on the effect of heat treatment at different temperatures of 900, 1000, and 1100°C with different holding times on the anisotropy of the printed samples to determine the conditions under which this inherent property is lost.

2. Materials and Methods

2.1. 316L stainless steel

In this study, the gas-atomized powder of 316L stainless steel, with the chemical composition presented in Table 1, was used as the raw material which is in good agreement with the reported values for AISI 316L and its adopted for the LPBF process [3].

2.2. Laser-based powder bed fusion (LPBF)

The 316L stainless steel rectangular cubic-shaped samples (Fig. 1) with dimensions of (6×20×30 mm³) were manufactured using the LPBF method with an AM250 LPBF machine from Renishaw. The

Table 1- Chemical composition of the AISI 316L austenitic stainless steel powder

Element	C	Mo	Ni	Mn	Cr	Si	Fe
Composition (wt.%)	0.006	2.5	12.5	1.5	16.6	0.7	Balance

details regarding the optimized manufacturing parameters of the LPBF process are provided in Table 2. As shown in Fig. 1, a vertical sample with the long side aligned with the building direction was printed using a scanning strategy with the 67° rotation of the scanning direction between layers.

2.3. Heat treatment

To examine the effect of annealing treatment, the as-built sample was cut into smaller pieces (6×10×10 mm³). Initially, the furnace was heated to 900, 1000, and 1100°C from room temperature, and the samples were placed in a preheated Exciton furnace for 3h, 4h, 5h, and 6h, followed by water quenching.

2.4. Characterizations

The surfaces of the as-built and heat-treated samples were prepared using 180-3000 SiC grinding papers, followed by fine polishing with a 0.05 alumina paste dispersed in water. Then the samples were subjected to electrolytic etching using a 10% oxalic acid solution, under a potential difference of 10V for 70 seconds to visualize the underlying microstructure [10, 28, 29]. To eliminate alumina particles from the surface, the samples were placed in a vessel containing acetone and then exposed to ultrasonic waves at a frequency of 37 kHz at a temperature of 30°C for 30 minutes in an Elma/P series ultrasonic bath. An optical microscope (OM) and scanning electron microscope (SEM)

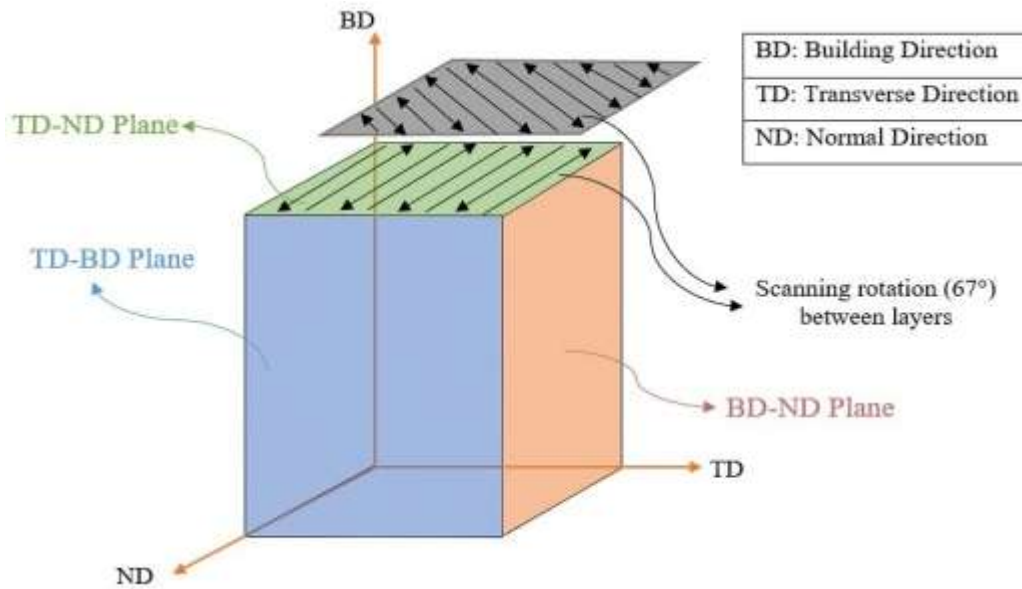


Fig. 1- Schematic of the specimens.

Table 2- LPBF process parameters used for sample fabrication

Parameter	Value
Laser power (W)	100-180
Layer thickness (µm)	40
Powder density (g cm ⁻³)	4.29
Width of molten pool (µm)	115
Exposure time (µs)	80
Scan line spacing (µm)	65

were used to examine the microstructure. Also, the Vickers microhardness tests were carried out on the as-built and heat-treated samples using a Coop/MH1 machine.

3. Results and discussion

3.1. Microstructure

The samples produced by the LPBF process exhibit certain inherent defects, such as voids and unmelted powders, which reduce their mechanical properties. These voids are typically several micrometers in size. Fig. 2 shows the presence of unmelted powders, indicated by white arrows, and two different types of porosity: keyhole porosity and gas entrapment porosity, marked by red and yellow circles, respectively. The presence of porosities is due to the high scanning speed combined with powder vaporization or extremely low or high beam power [30, 31].

A comprehensive representation of the microstructure of the as-built sample is exhibited in Fig. 3, which shows the melt pool boundaries, cellular sub-structure, and elongated and equiaxed austenitic grains. This Figure reveals the microstructure of three different sections, TD-ND, TD-BD, and BD-ND planes. The TD-ND plane reveals the manufacturing process, with overlapping laser scans resulting in a network of melt pools. In contrast, the parallel planes to the building platform (TD-BD and BD-ND) display a structure influenced by the laser-scanning pattern, marked by regions that have been molten and solidified rapidly. Fig. 3 (a) shows the OM image of the as-built sample on the TD-ND plane, which contains equiaxed grains with melt pool boundaries rotated 67° between the layers. The observed equiaxed grains with an average diameter of 25 μm are the transverse cross-section of elongated grains oriented in the building direction. Additionally, residual stress was the driving force for the formation of equiaxed grains generated due to the rapid heating and cooling rate of the microstructure during the fabrication of samples, which was in good agreement with [17, 24]. Fig. 3 (a) shows some laser tracks exhibit inconsistency and it caused to creation of short elliptical melt tracks. The phenomenon of unstable melt tracks is induced by the disturbance of the molten pool during selective laser melting. Some porosity and unmelted powders are shown in Figs. 3 (a) and (c), respectively. Additionally, Figs. 3 (c) and (e) illustrate dome-like melt pool boundaries on TD-BD and BD-ND planes. It is interesting to note that in some regions, the interconnection boundaries generated through the fusion of layers that are called layer-layer melt pool boundaries, as well as some other melt pools indicate the extent of overlap between neighboring scanning trajectories

which are called track-track melt pool boundaries. The size of the melt pool like depth and width differ significantly from one another. According to Casati et al. [32] various parameters play a significant role in determining the size of the melt pools such as the input power, the exposure time, the beam size, and spot size which also affect the growth directions of grains. Figs. 3 (b), (d), and (f) show the SEM images of the as-built specimens in different planes. These images show layer patterns and the formation of columnar and equiaxed cell structures in various sizes and shapes. As shown in Fig. 3 (b) particles like se phases and oxide inclusions are distributed in some areas of the as-built microstructure. These particles are shown with yellow arrows. According to Zhong et al. [33] the presence of oxide particles can be attributed to the chamber gas and the initial powder, which contains a thin oxide layer that melts when exposed to the laser. Also, Morozova et al. [24] reported the presence of α -ferrite inclusions in the as-built microstructure, which were not observed in this study. In addition, the elongated cellular structures are attributed to the different growth directions of the columnar grains in which they are located. Also, According to Wang et al. [34] both temperature gradient (G) and growth rate (R) play vital roles in determining the variation of structural morphology (planar, cellular, or columnar). Due to the parallelism of the heat source with the heat flow at the center of the melt pools, the growth rate increases sharply; therefore, as Fig. 3 (f) shows the G/R ratio decreases and the equiaxed cellular structures become more pronounced. Additionally, the increase in $G \times R$ results in smaller dislocation cell sizes and higher dislocation density at the dislocation cell boundaries, resulting in higher hardness value. The higher magnification of equiaxed and columnar cellular structures on the TD-BD Plane compared in Fig. 4.

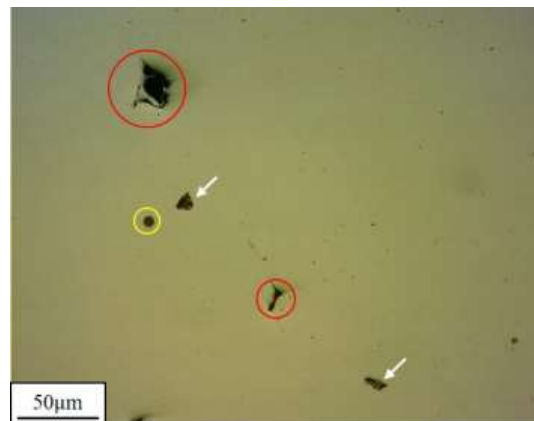


Fig. 2- Various defects in 316L stainless steel sample produced by laser-based powder bed fusion.

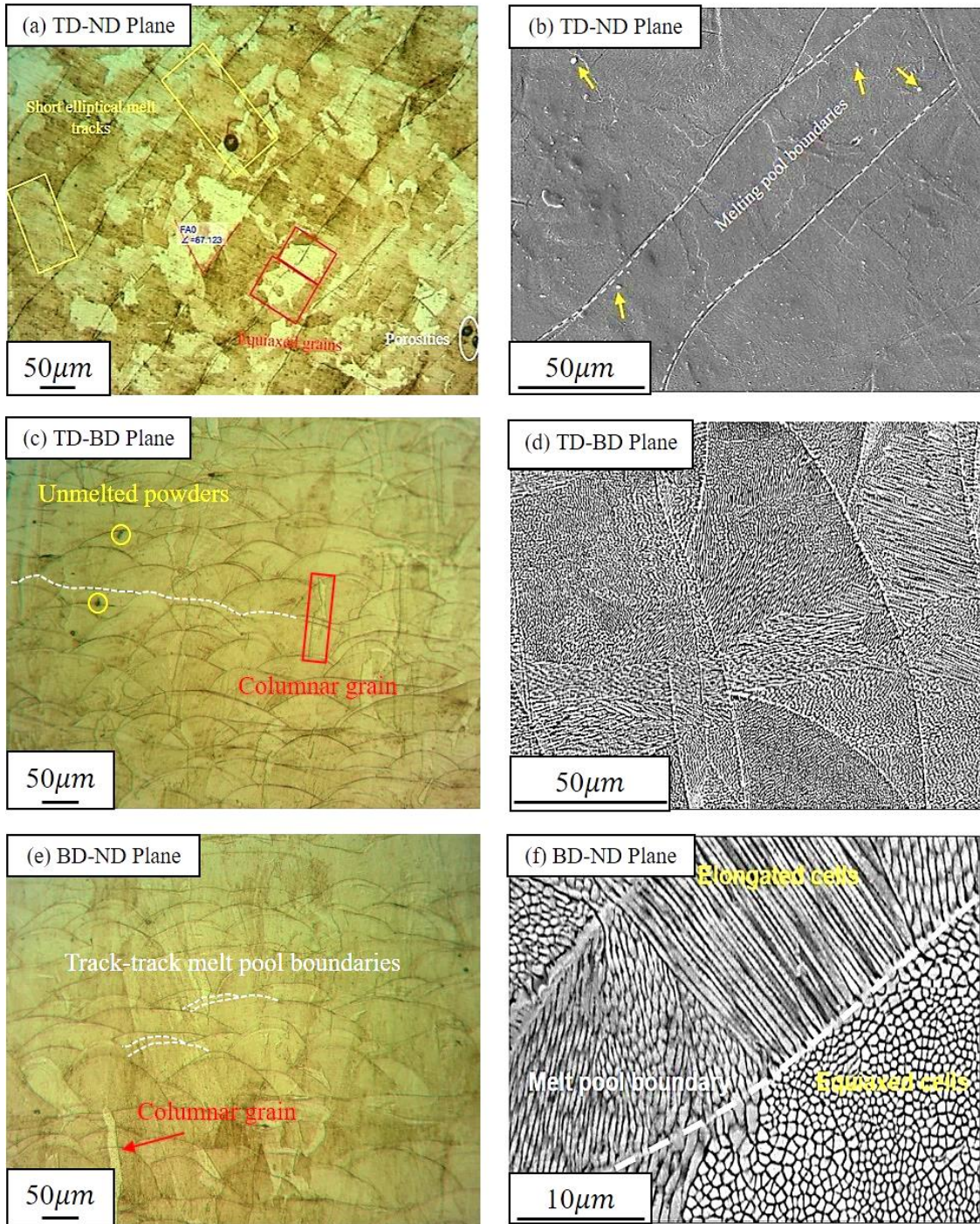


Fig. 3- Microscope images (a, c, e) optical and (b, d, f) scanning electron of 316L stainless steel produced by laser powder bed fusion.

After annealing at 900°C for different holding times, the as-built microstructure changed significantly. Fig. 5 (a) shows the heat-treated microstructure for 3h. The thickness of the laser tracks has been reduced sharply, as compared to the as-built sample; these tracks are much lighter in color, indicating a slight homogenization of the structure, which results in a decrease in hardness during the initial stages of the heat treatment. These tracks are indicated with yellow arrows. Therefore, the presence of the laser tracks as well as melt pool boundaries indicate insufficient heat treatment time and incomplete recrystallization of the structure. However, by increasing the annealing time to 4h, the microstructure changed noticeably. Fig. 5 (b) shows due to the chemical homogenization and diffusion at higher holding times, both melt pool boundaries and laser tracks have vanished. It is worth noting that in the samples, which were produced using the LPBF process due to the higher heating and cooling rates, the local misorientation is sufficiently high, and stored energy will increase rapidly, therefore; the critical size of nuclei drop sharply and the recrystallized grains will be obvious. These grains are shown with white arrows. Additionally, in some areas of Fig. 5 (b), smaller-sized grains are also

observed. The presence of these grains indicates the intersection of laser tracks between the previous (n-1) and subsequent (n) layers during the LPBF process [28]. As a result, grains with significantly smaller dimensions compared to other grains in the microstructure become apparent. These grains are indicated with red arrows. Fig. 5 (c) shows by reaching the annealing time to 5h, the grain boundary structures have become more defined, and cellular structures have transformed into equiaxed grains. These grains are more pronounced compared to those subjected to 4h of heat treatment, indicating an increased fraction of recrystallization during the extended heat treatment period. Moreover, according to some researchers, nano inclusions precipitate along the melt pools and cellular structures by increasing heat treatment time, therefore; both thermal stability and hardness value will increase [35, 36]. According to Fig. 5 (d), increasing the heat treatment duration to 6h, significantly increased both the volume fraction and size of equiaxed grains, indicating a higher degree of homogenization and recrystallization, accompanied by grain growth. Due to several reasons, the shape and structure of the equiaxed grains in samples produced by the LPBF

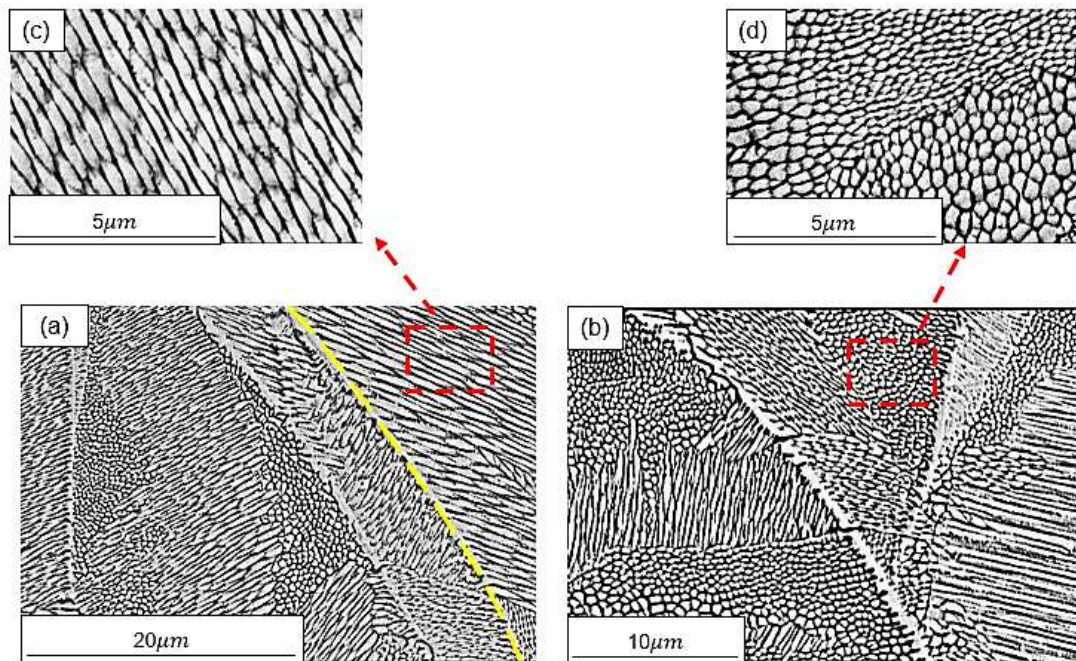


Fig. 4- Scanning electron microscopy images on TD-BD plane at different magnifications. (a, c) melt pool boundary (yellow dash line) and elongated cell structures, and (b, d) low and high magnification of equiaxed cell structures in melt pool.

process are significantly different from those in conventionally produced samples. These observed differences can be attributed to the rapid heating and cooling rates [37] during production and the distinct solidification front, particularly in samples produced by the LPBF process. Another factor that plays an important role is the low temperature and higher holding time of the heat treatment in this study.

Increasing the temperature and the holding time can enhance the volume fraction of equiaxed grains. Based on optical images in Figs. 5 (b), (c), and (d) it can be concluded that the recrystallized grains have formed in different areas. Additionally, the presence of secondary phase particles on cell and grain boundaries over extended annealing times has led to the zener pinning effect and incomplete recrystallized grains in some areas of the microstructure. It is worth noting that this phenomenon is one of the most effective mechanisms for experiencing sluggish recrystallization in alloys. Both Fig. 6 and Fig. 7 ((a) and (b)) show the SEM image and the Energy Dispersive Spectroscopy (EDS) analysis respectively annealed at 900°C for 5h. At this annealing time and temperature, the

carbide particles precipitated in grains and along the grain boundaries, which is expected to lead to thermal stability and increase the average hardness value.

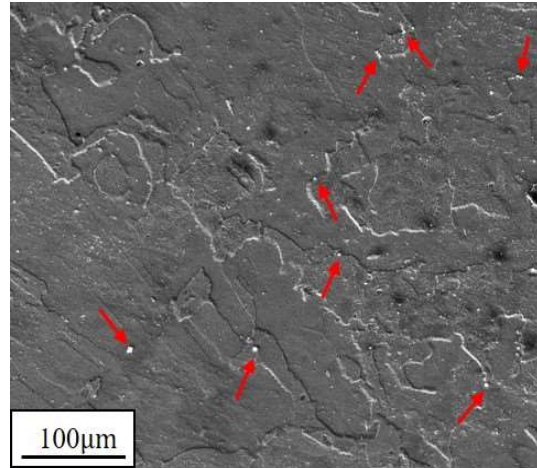


Fig. 6- SEM image of the TD-ND plane after annealing at 900°C for 5h.

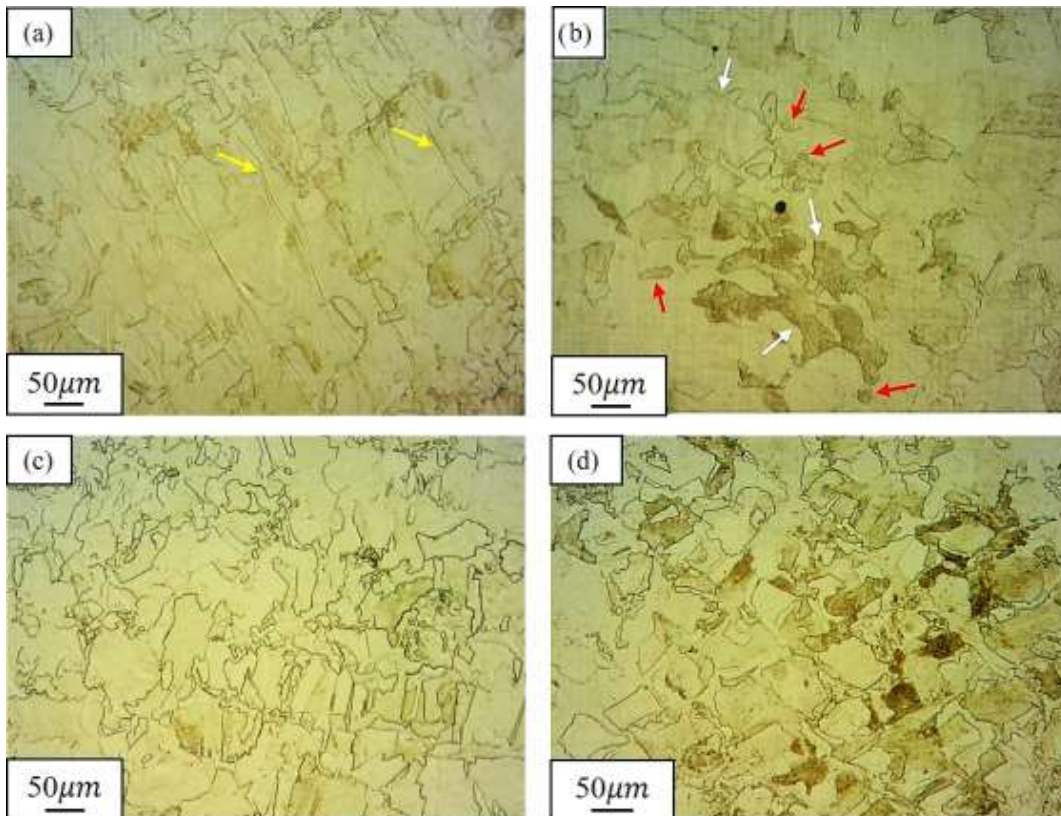


Fig. 5- OM images of the TD-ND plane after annealing at 900°C for (a) 3h, (b) 4h, (c) 5h and (d) 6h.

Fig. 7 (a) illustrates the distribution of elements like Cr, Mn, Fe, Ni, and Mo that were uniform. Moreover, the table of elemental distribution in Fig. 7 (b) shows that the main reason for the increase in hardness values is almost the formation of carbides, which is indicated by the black arrow. It is worth noting that, at this temperature, carbides can form compounds such as Mo_2C , Cr_{23}C_6 , Cr_3C_2 , and M_6C usually nucleate on grain boundaries and intragranular sites at different temperature ranges from 400 to 900°C [38, 39]. These elements are randomly distributed in the matrix in the form of spherical particles after annealing at this temperature and time. In addition, the SEM image in Fig. 8 illustrates the sample annealed at 900°C for 6h, indicating the presence of carbide particles (red circles) on grain boundaries.

to Roirand et al. [40] during the fabrication of the sample by the LPBF process, heavy elements such as Cr, Mo, and Si which are present in 316L stainless steel powder, residue on the dislocation cell boundaries. With an increase in temperature to 750-800°C for 2h, due to the activation of the diffusion phenomenon, these elements will precipitate on the triple junction grain boundaries and within the grains. By increasing the temperature to 1000-1200°C the diffusion rate of these elements on the triple junction grain boundaries increases, leading to the growth of the precipitate dimensions, eventually surrounding all the grain boundaries. Moreover, precipitates and secondary phases on the grain boundaries and within the grains indicate the near elimination of dislocation cells.

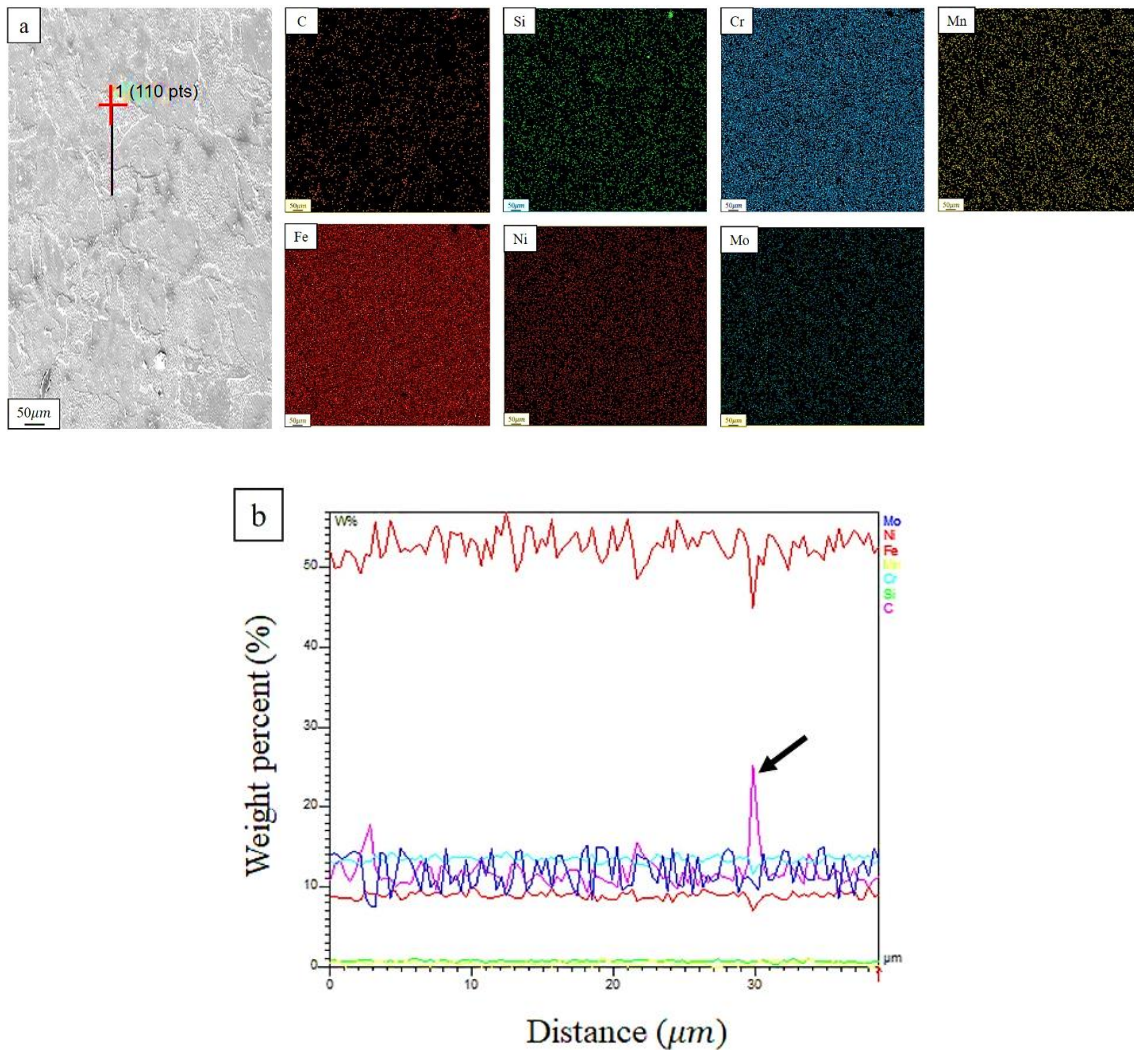


Fig. 7- (a) SEM micrograph on 316L stainless steel with corresponding elemental map, and (b) line scan of elemental distribution.

After analysis of the microstructure changes at various annealing times, additional samples were annealed at 1000 and 1100°C for 4h to investigate the effects of different annealing temperatures. The resulting changes are illustrated in Fig. 9. Fig. 9 (a) shows with temperature elevation to 1000°C, the volume fraction of equiaxed grains increased, indicating a higher fraction of recrystallization at this annealing temperature and time. Additionally, at this temperature and time, the increased volume fraction of recrystallized grains led to greater microstructural homogenization compared to annealing at 900°C for 4h, resulting in the approximate absence of carbide particles, and a decrease in the average hardness on all three TD-ND, TD-BD, and BD-ND planes. As shown in Fig. 9 (b), once the temperature was increased to 1100°C for 4h, the resulting equiaxed grain structure resembled that of conventionally processed samples, producing a uniform microstructure without columnar grains. In addition, the size of these grains increased significantly due to the higher temperature. Also, thermal twins were observed in the annealing grains at this temperature and time showing the softening phenomena (indicated by yellow arrows).

3.2. Microhardness measurements

The average microhardness of the as-built sample on the TD-ND plane was around 256 HV0.2 which was in perfect agreement with the documented value in the literature [41]. In addition, the average microhardness of 316L stainless steel on TD-BD and BD-ND planes were around 271 and 242 HV0.2 respectively. According to Lu et al. [42] the rapid heating and cooling rates in the LPBF process result in the formation of elongated grains in the microstructures with different dimensions on TD-ND, TD-BD, and BD-ND planes that are distributed regardless of plane orientation. Therefore, due

to these variations, the hardness values on these planes differed, and the anisotropy was evident. According to Chen et al. [25] the disappearance of cellular structures begins above 400°C, also Chao et al. [26] mentioned that the cellular substructure reached complete decomposition at the annealing temperature of 800°C. In this research after annealing at 900°C for 3h, the annihilation of dislocations and diffusion of elements occurred; therefore, the average microhardness on the TD-ND plane (perpendicular to the building direction) plunged to 199 HV0.2.

Fig. 10 (a) shows the variations in hardness over annealing time on the TD-ND plane. The average hardness values at 4h, 5h, and 6h were 195, 203, and 226 HV0.2, respectively. Fig. 10 illustrates that the hardness increased after 4h of annealing at 900°C.

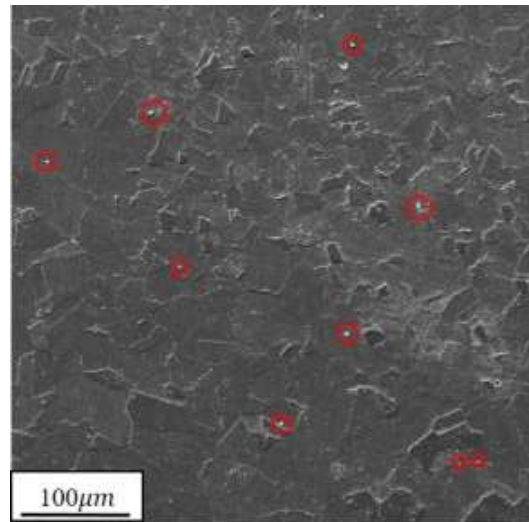


Fig. 8- SEM image of carbide particles on the TD-ND plane heat-treated at 900°C for 6h.

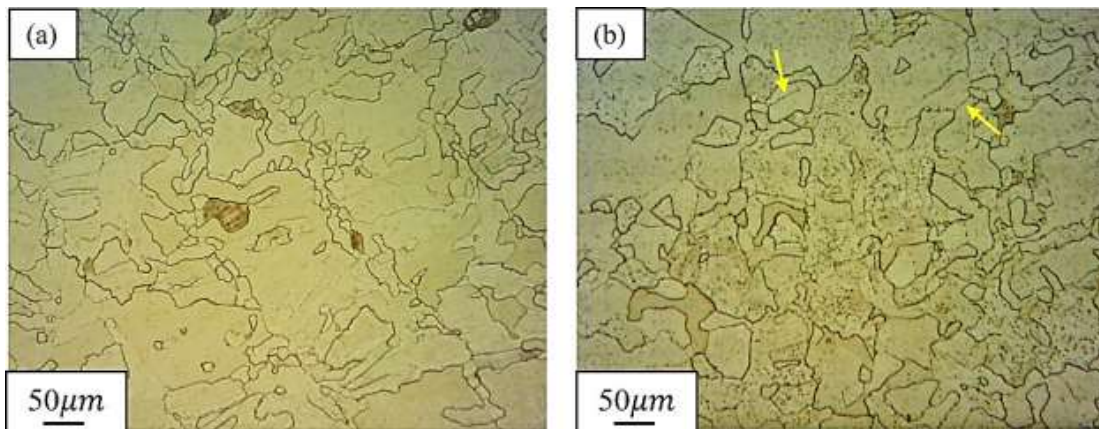


Fig. 9- OM images of the TD-ND plane after annealing for 4h at (a) 1000°C and (b) 1100°C.

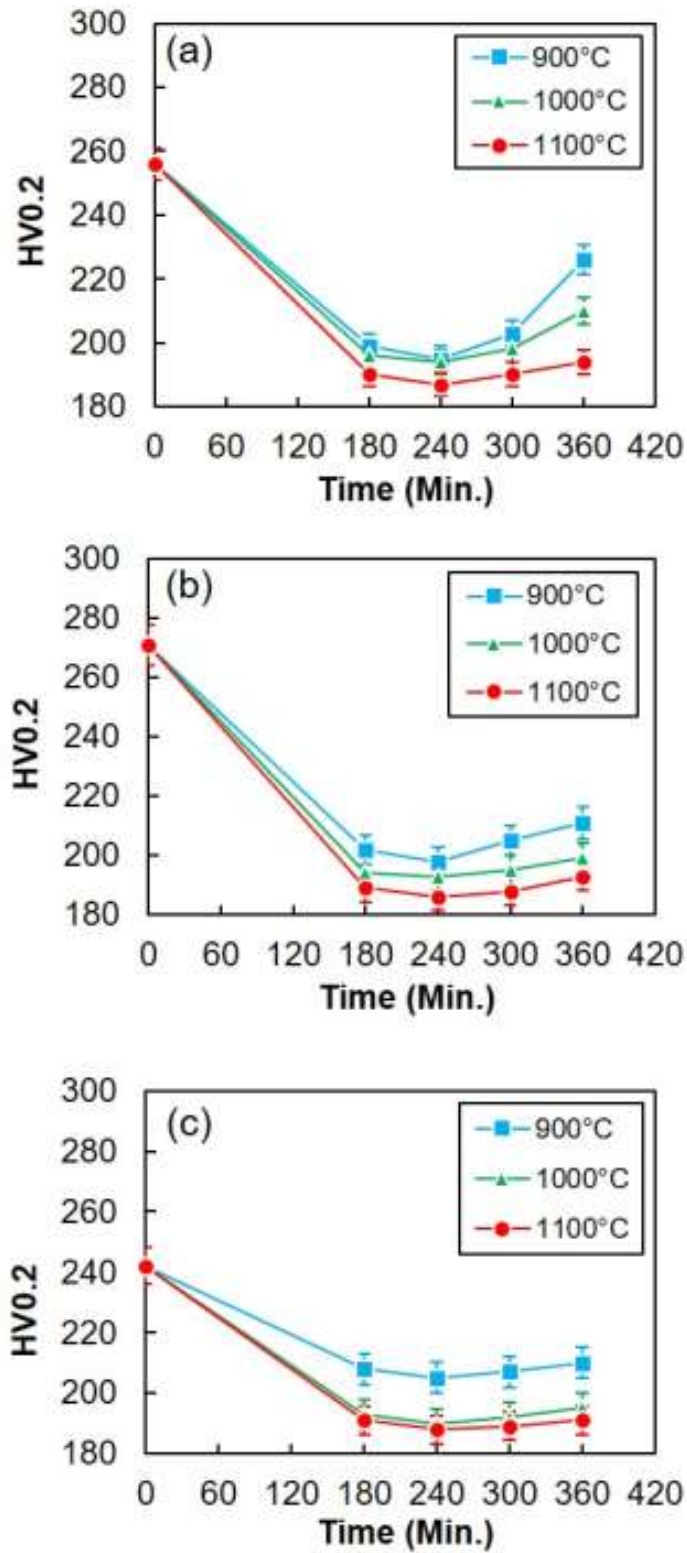


Fig. 10- The hardness variation of the annealed samples at 900°C,1000°C, and 1100°C for 3h up to 6h on (a) TD-ND, (b) TD-BD, and (c) BD-ND planes.

This observation was attributed to forming carbide particles within the microstructure, depicted in the SEM images in Fig. 6, and reported that after annealing at 900 for 5h, the carbide particles formed in the microstructure with an average diameter of 0.469 nanometers. As shown in Fig. 10 (b), the average hardness value on the TD-BD plane decreased to 198HV0.2 after annealing at 900°C for 4h. However, with a longer annealing time, the average hardness rose to 205HV0.2. Other studies have mentioned the formation of precipitates and oxide particles along grain boundaries at 900°C, which might account for the increased hardness during longer annealing time [35]. Also, Fig. 10 (c) shows similar changes in hardness values on the BD-ND plane.

In addition, Fig. 11 showed the effect of annealing at higher temperatures (1000°C and 1100°C) on microhardness. The microhardness behavior showed that increasing the temperature from 900°C to 1100°C did not lead to a significant increase in microhardness values compared to 900°C, due to the dissolution of carbide particles in the matrix at higher temperatures. To investigate the hardness changes by annealing at 900, 1000, and 1100°C for 4h, the hardness diagram based on annealing temperatures is shown in Fig. 11 on TD-ND, TD-BD, and BD-ND planes. This diagram shows a noticeable drop in microhardness value at 1100°C, which aligns well with the OM image shown in Fig. 9 (b). This microstructure shows the size of grains increased as compared to microstructural

changes at temperatures like 900°C, and 1000°C. Moreover, at this annealing temperature and time (1100°C for 4h), the hardness values became very similar (186-188 HV0.2), suggesting that the anisotropic properties of the fabricated samples have disappeared and the structure has completely recrystallized.

4. Conclusions

The 316L stainless steel samples produced using the LPBF process were exposed to PMHT within a temperature range of 900-1100°C, with different holding times. The correlations between heat treatment, and anisotropy behavior were investigated. The main results are as follows:

1. The 316L stainless steel samples produced via the LPBF process exhibited distinct microstructural variations across planes due to differences in cooling rates. The TD-ND plane displayed fine, uniform equiaxed grains, while other planes were characterized by coarser, columnar structures. These variations significantly affected the mechanical properties, but annealing could effectively reduce defects and anisotropy, thereby improving material performance.

2. By annealing the samples at 900°C for 3h, 4h, 5h, and 6h, the anisotropic behavior of the produced samples decreased gradually due to the elimination of porosities, disappearance of melt pool boundaries, formation of recrystallized grains, and elimination of dislocation cell structures due to the annihilation of dislocations align the cell boundaries.

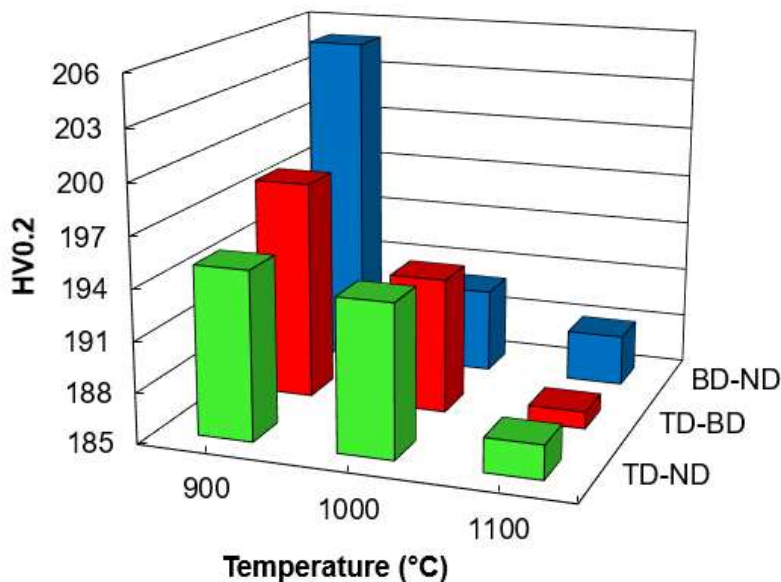


Fig. 11- The hardness variation of the samples annealed for 4h as a function of temperature on the TD-ND, TD-BD, and BD-ND planes.

3. Increasing temperature to 1000 and 1100°C for 4h, due to the recrystallization in microstructure and disappearance of columnar grains, the fraction of equiaxed grains at 1100°C was higher than at 1000°C. Additionally, annealing twins were observed at 1100°C.

4. Based on the hardness measurements at 900°C over various holding times, 4h, which showed the lowest average hardness, was identified as the optimal time needed for structural homogenization at higher temperatures. By annealing at 1000 and 1100°C, we identified annealing at 1100°C for 4h as the proper temperature and holding time for eliminating anisotropy and achieving full structural homogenization.

References

1. A. Saboori, A. Aversa, G. Marchese, S. Biamino, M. Lombardi, and P. Fino, "Microstructure and mechanical properties of AISI 316L produced by directed energy deposition-based additive manufacturing: A review," *Applied sciences*, vol. 10, no. 9, pp. 3310, 2020.
2. S. Bahl, S. Mishra, K. Yazar, I. R. Kola, K. Chatterjee, and S. Suwas, "Non-equilibrium microstructure, crystallographic texture and morphological texture synergistically result in unusual mechanical properties of 3D printed 316L stainless steel," *Additive Manufacturing*, vol. 28, pp. 65-77, 2019.
3. X. Liang, "High cycle fatigue behavior of additive manufactured stainless steel 316L: free surface effect and microstructural heterogeneity," HESAM Université, 2020.
4. C. Keller, K. Tabalaiev, G. Marnier, J. Noudem, X. Sauvage, and E. Hug, "Influence of spark plasma sintering conditions on the sintering and functional properties of an ultra-fine grained 316L stainless steel obtained from ball-milled powder," *Materials Science and Engineering: A*, vol. 665, pp. 125-134, 2016.
5. D. Landolt, *Corrosion and surface chemistry of metals*: EPFL press, 2007.
6. M. Naghizadeh, and H. Mirzadeh, "Elucidating the effect of alloying elements on the behavior of austenitic stainless steels at elevated temperatures," *Metallurgical and Materials Transactions A*, vol. 47, pp. 5698-5703, 2016.
7. K. Saeidi, and F. Akhtar, "Microstructure-tailored stainless steels with high mechanical performance at elevated temperature," *Stainless Steels and Alloys*: IntechOpen London, UK, 2018.
8. T. DebRoy, H. L. Wei, J. S. Zuback, T. Mukherjee, J. W. Elmer, J. O. Milewski, A. M. Beese, A. d. Wilson-Heid, A. De, and W. Zhang, "Additive manufacturing of metallic components—process, structure and properties," *Progress in Materials Science*, vol. 92, pp. 112-224, 2018.
9. J. P. Oliveira, A. LaLonde, and J. Ma, "Processing parameters in laser powder bed fusion metal additive manufacturing," *Materials & Design*, vol. 193, pp. 108762, 2020.
10. T. Ronneberg, C. M. Davies, and P. A. Hooper, "Revealing relationships between porosity, microstructure and mechanical properties of laser powder bed fusion 316L stainless steel through heat treatment," *Materials & Design*, vol. 189, pp. 108481, 2020.
11. W. Abd-Elaziem, S. Elkatatny, A.-E. Abd-Elaziem, M. Khedr, M. A. Abd El-baky, M. A. Hassan, M. Abu-Okail, M. Mohammed, A. Järvenpää, and T. Allam, "On the current research progress of metallic materials fabricated by laser powder bed fusion process: a review," *Journal of Materials Research and Technology*, vol. 20, pp. 681-707, 2022.
12. W. J. Sames, F. List, S. Pannala, R. R. Dehoff, and S. S. Babu, "The metallurgy and processing science of metal additive manufacturing," *International materials reviews*, vol. 61, no. 5, pp. 315-360, 2016.
13. M. Brandt, "Laser additive manufacturing: materials, design, technologies, and applications," 2016.
14. L. Hitzler, C. Janousch, J. Schanz, M. Merkel, B. Heine, F. Mack, W. Hall, and A. Öchsner, "Direction and location dependency of selective laser melted AISi10Mg specimens," *Journal of Materials Processing Technology*, vol. 243, pp. 48-61, 2017.
15. R. Shrestha, J. Simsiwong, N. Shamsaei, S. M. Thompson, and L. Bian, "Effect of build orientation on the fatigue behavior of stainless steel 316L manufactured via a laser-powder bed fusion process," 2016.
16. S. Mohammadzahi, and H. Mirzadeh, "Grain refinement of austenitic stainless steels by cross rolling and annealing treatment: A review," *Journal of Ultrafine Grained and Nanostructured Materials*, vol. 57, no. 2, pp. 112-119, 2024.
17. A. Taghipour, Y. Mazaheri, J. McDavid, S. Sheikhi, M. Braun, J. Shen, B. Klusemann, and S. Ehlers, "Strengthening Mechanisms and Strain Hardening Behavior of 316L Stainless Steel Manufactured by Laser-Based Powder Bed Fusion," *Advanced Engineering Materials*, vol. 25, no. 4, pp. 2201230, 2023.
18. D. Kumar, G. Shankar, K. Prashanth, and S. Suwas, "Texture dependent strain hardening in additively manufactured stainless steel 316L," *Materials Science and Engineering: A*, vol. 820, pp. 141483, 2021.
19. T. M. Mower, and M. J. Long, "Mechanical behavior of additive manufactured, powder-bed laser-fused materials," *Materials Science and Engineering: A*, vol. 651, pp. 198-213, 2016.
20. Z. Baicheng, L. Xiaohua, B. Jiaming, G. Junfeng, W. Pan, S. Chen-nan, N. Muiling, Q. Guojun, and W. Jun, "Study of selective laser melting (SLM) Inconel 718 part surface improvement by electrochemical polishing," *Materials & Design*, vol. 116, pp. 531-537, 2017.
21. B. J. M. Freitas, V. A. de Oliveira, P. Gargarella, G. Y. Koga, and C. Bolfarini, "Microstructural characterization and wear resistance of boride-reinforced steel coatings produced by Selective Laser Melting (SLM)," *Surface and Coatings Technology*, vol. 426, pp. 127779, 2021.
22. A. Charmi, R. Falkenberg, L. Ávila, G. Mohr, K. Sommer, A. Ulbricht, M. Sprengel, R. S. Neumann, B. Skrotzki, and A. Evans, "Mechanical anisotropy of additively manufactured stainless steel 316L: An experimental and numerical study," *Materials Science and Engineering: A*, vol. 799, pp. 140154, 2021.
23. L. Hitzler, J. Hirsch, B. Heine, M. Merkel, W. Hall, and A. Öchsner, "On the anisotropic mechanical properties of selective laser-melted stainless steel," *Materials*, vol. 10, no. 10, pp. 1136, 2017.
24. I. Morozova, C. Kehm, A. Obrosof, Y. Yang, K. U. M. Miah, E. Uludintceva, S. Fritzsche, S. Weiß, and V. Michailov, "On the Heat Treatment of Selective-Laser-Melted 316L," *Journal of Materials Engineering and Performance*, vol. 32, no. 10, pp. 4295-4305, 2023.
25. N. Chen, G. Ma, W. Zhu, A. Godfrey, Z. Shen, G. Wu, and X. Huang, "Enhancement of an additive-manufactured austenitic stainless steel by post-manufacture heat-treatment," *Materials Science and Engineering: A*, vol. 759, pp. 65-69, 2019.
26. Q. Chao, S. Thomas, N. Birbilis, P. Cizek, P. D. Hodgson, and D. Fabijanic, "The effect of post-processing heat treatment on the microstructure, residual stress and mechanical properties of selective laser melted 316L stainless steel," *Materials Science and Engineering: A*, vol. 821, pp. 141611, 2021.
27. W.-Y. Wang, A. Godfrey, and W. Liu, "Effect of heat treatment on microstructural evolution in additively manufactured 316L stainless steel," *Metals*, vol. 13, no. 6, pp. 1062, 2023.
28. F. Pinto, L. S. Aota, I. R. Souza Filho, D. Raabe, and H. R. Z. Sandim, "Recrystallization in non-conventional microstructures of 316L stainless steel produced via laser powder-bed fusion: effect of particle coarsening kinetics," *Journal of Materials Science*, vol. 57, no. 21, pp. 9576-9598, 2022.

29. E. de Sonis, S. Dépinoy, P.-F. Giroux, H. Maskrot, L. Lemarquis, O. Hercher, F. Villaret, and A.-F. Gourgues-Lorenzon, "Dependency of recrystallization kinetics on the solidification microstructure of 316L stainless steel processed by laser powder bed fusion (LPBF)," *Materials Characterization*, vol. 194, pp. 112370, 2022.
30. J. Gholamzadeh, S. M. Fatemi, N. Mollaei, and A. Abedi, "Processing of Ultrafine/nano-grained microstructures through additive manufacturing techniques: a critical review," *Journal of Ultrafine Grained and Nanostructured Materials*, vol. 57, no. 2, pp. 203-221, 2024.
31. J. L. Tan, C. Tang, and C. H. Wong, "A computational study on porosity evolution in parts produced by selective laser melting," *Metallurgical and Materials Transactions A*, vol. 49, pp. 3663-3673, 2018.
32. R. Casati, J. Lemke, and M. Vedani, "Microstructure and fracture behavior of 316L austenitic stainless steel produced by selective laser melting," *Journal of Materials Science & Technology*, vol. 32, no. 8, pp. 738-744, 2016.
33. Y. Zhong, L. Liu, S. Wikman, D. Cui, and Z. Shen, "Intragranular cellular segregation network structure strengthening 316L stainless steel prepared by selective laser melting," *Journal of Nuclear Materials*, vol. 470, pp. 170-178, 2016.
34. D. Wang, C. Song, Y. Yang, and Y. Bai, "Investigation of crystal growth mechanism during selective laser melting and mechanical property characterization of 316L stainless steel parts," *Materials & Design*, vol. 100, pp. 291-299, 2016.
35. K. Chadha, Y. Tian, J. G. Spray, and C. Aranas Jr, "Effect of annealing heat treatment on the microstructural evolution and mechanical properties of hot isostatic pressed 316L stainless steel fabricated by laser powder bed fusion," *Metals*, vol. 10, no. 6, pp. 753, 2020.
36. P. Deng, H. Yin, M. Song, D. Li, Y. Zheng, B. C. Prorok, and X. Lou, "On the thermal stability of dislocation cellular structures in additively manufactured austenitic stainless steels: roles of heavy element segregation and stacking fault energy," *JOM*, vol. 72, pp. 4232-4243, 2020.
37. C. Hopper, C. I. Pruncu, P. A. Hooper, Z. Tan, S.-T. Yang, Y. Liu, and J. Jiang, "The effects of hot forging on the preform additive manufactured 316 stainless steel parts," *Micron*, vol. 143, pp. 103026, 2021.
38. B. Weiss, and R. Stickler, "Phase instabilities during high temperature exposure of 316 austenitic stainless steel," *Metallurgical and Materials Transactions B*, vol. 3, pp. 851-866, 1972.
39. G. Tapia, and A. Elwany, "A review on process monitoring and control in metal-based additive manufacturing," *Journal of Manufacturing Science and Engineering*, vol. 136, no. 6, pp. 060801, 2014.
40. H. Roirand, A. Pugliara, B. Malard, A. Hor, and N. Saintier, "Multiscale study of additively manufactured 316 L microstructure sensitivity to heat treatment over a wide temperature range," *Materials Characterization*, vol. 208, pp. 113603, 2024.
41. Y. Liu, D. Xie, and F. Lv, "Strength Enhancement of Laser Powder Bed Fusion 316L by Addition of Nano TiC Particles," *Materials*, vol. 17, no. 5, pp. 1129, 2024.
42. Y. Lu, H. Zhang, P. Xue, L. Wu, F. Liu, L. Jia, D. Ni, B. Xiao, and Z. Ma, "Microstructural Evaluation and Tensile Properties of Al-Mg-Sc-Zr Alloys Prepared by LPBF," *Crystals*, vol. 13, no. 6, pp. 913, 2023.